Article

# Efficient Formation of Light-Absorbing Polymeric Nanoparticles from the Reaction of Soluble Fe(III) with C4 and C6 Dicarboxylic Acids

Ashley Tran,[†] Geoffrey Williams,[†] Shagufta Younus,[†] Nujhat N. Ali,[‡] Sandra L. Blair,[‡] Sergey A. Nizkorodov,[‡] and Hind A. Al-Abadleh*,[†]

[†]Department of Chemistry and Biochemistry, Wilfrid Laurier University, Waterloo, ON N2L 3C5, Canada
[‡]Department of Chemistry, University of California, Irvine, California 92697, United States

**S** *Supporting Information*

**ABSTRACT:** The role of transition metals in the formation and aging of secondary organic aerosol (SOA) from aliphatic and aromatic precursors in heterogeneous/multiphase reactions is not well understood. The reactivity of soluble Fe(III) toward known benzene photooxidation products that include fumaric (*trans*-butenedioic) and muconic (*trans*,*trans*-2,4-hexadienedioic) acids was investigated. Efficient formation of brightly colored nanoparticles was observed that are mostly rod- or irregular-shaped depending on the structure of the organic precursor. The particles were characterized for their optical properties, growth rate, elemental composition, iron content, and oxidation state. Results indicate that these particles have mass absorption coefficients on the same order as black carbon and larger than that of biomass burning aerosols. The particles are also amorphous in nature and consist of polymeric chains of Fe centers complexed to carboxylate groups. The oxidation state of Fe was found to be in between Fe(III) and Fe(II) in standard compounds. The organic reactant to iron molar ratio and pH were found to affect the particle growth rate. Control experiments using maleic acid (*cis*-butenedioic acid) and succinic acid (butanedioic acid) produced no particles. The formation of particles reported herein could account for new pathways that lead to SOA and brown carbon formation mediated by transition metals. In addition, the multiple chemically active components in these particles (iron, organics, and acidic groups) may have an effect on their chemical reactivity (enhanced uptake of trace gases, catalysis, and production of reactive oxygen species) and their likely poor cloud/ice nucleation properties.
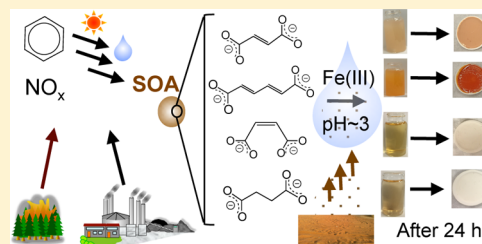
## ■ INTRODUCTION

Secondary organic aerosols (SOAs) are produced by atmospheric oxidation of volatile organic compounds (VOCs) from biogenic and anthropogenic sources followed by condensation of the VOC oxidation products on pre-existing particles. The freshly produced SOAs undergo chemical aging as a result of surface and bulk reactions, which change the climate and health effects of SOAs.[1] For example, photochemical aging of SOAs can change both the real[2] and imaginary[3] parts of the refractive index. A number of aging processes produce SOA compounds that absorb near-UV and visible radiation, known collectively as "brown carbon".[4,5] Examples include photooxidation of aromatic compounds, aqueous photooxidation of phenols, and reactions of glyoxal and methylglyoxal with ammonium sulfate (see Laskin et al.[4] and references therein).

The role of transition metals in the aging and formation of SOAs and brown carbon from aliphatic and aromatic precursors in heterogeneous/multiphase reactions is not well understood.[6–8] In particular, iron (Fe) drives redox chemistry and forms complexes with a number of organic and inorganic ligands in the bulk aqueous phase and at the interface.[8] Iron is a major component of naturally emitted mineral dust[9–11] and particles from anthropogenic[12] and biomass burning emissions.[13,14] Single particle analysis of field-collected aerosols from marine, urban, and rural sites reported concentrations of soluble and insoluble iron.[15–26] Schroth et al.[27] demonstrated that iron speciation (oxidation state and bonding environment) varies by aerosol source. For example, soils in arid regions are dominated by Fe(III)-(oxyhydr)oxides, glacial weathered-particles by Fe-(II)-silicates, and oil fly ash from fossil fuel combustion by Fe(III) sulfates. Cycling between wet aerosols characterized by highly acidic conditions with a few layers of adsorbed water, and cloud droplets characterized by more pH-neutral conditions, was shown to affect the concentration of dissolved iron.[28] Insoluble iron dissolves readily under the acidic conditions relevant to wet aerosols, whereas under higher pH the dissolved iron precipitates as poorly crystalline nanoparticles. As a result of these aerosol–cloud interactions, long-range transport of mineral dust particles and uptake of acidic gases enhance the fraction of soluble iron in particles.[29] The ubiquitous presence of water in aerosol particles affects the pH, amount of soluble Fe, solute:solvent ratio, and therefore chemistry.[30]

We recently demonstrated that dark redox reactions of Fe with catechol and guaiacol (semivolatile phenolic compounds emitted from biomass burning and produced by photooxidation of

aromatic VOCs), under high solute:solvent ratio that mimic reactions in *adsorbed water*, lead to complex polymeric products that strongly absorb visible radiation.[31] The mass absorption coefficients of the products were as large as that reported for brown carbon from biomass burning.

Dicarboxylic acids can form complexes with soluble Fe, and if they are unsaturated, they can also participate in redox reactions. Ring-opening reactions involving common atmospheric aromatic compounds, such as benzene, toluene, and xylenes, are a known source of unsaturated aldehydes[32] and dicarboxylic acids.[33] In materials science, metal-catalyzed polymerization of diacids in the aqueous phase was reported earlier to form either amorphous polymers or metal organic frameworks (MOFs). For example, Apblett[34] patented a method for the formation of amorphous "iron coordination polymers for adsorption of arsenate and phosphate". The polymer was obtained from mixing aqueous solutions of sodium fumarate with iron chloride. Under conditions that optimize yield and particle shape, Lin et al.[35] reported the formation of crystalline iron-based MOF, MIL-88A, from the aqueous phase reaction of fumaric acid with $FeCl_3$ at 85 °C. Rorrer et al.[36] used Ti(IV) butoxide as a transesterification catalyst to form high molecular weight polymers from a mixture of *cic,cis*-muconic acid, succinic acid, and dialcohol oligomers. However, studies that explore the extent of iron-catalyzed polymerization of atmospherically relevant organics under conditions representative of multicomponent aerosols are still lacking.

The objective of this study is to explore the reactivity of soluble Fe with *trans*-unsaturated C4 and C6 diacids, namely, fumaric and muconic acids. For comparison, similar experiments are performed with *cis*-unsaturated and saturated diacids, namely, maleic and succinic acids. Muconic acid is identified as a product of photooxidation of benzene,[37,38] and fumaric, maleic, and succinic acids are commonly observed in the atmosphere.[39,40] We show fast formation of iron-containing polymeric organic nanoparticles upon reaction of Fe(III) with muconic and fumaric acids under acidic conditions using relatively high and low concentrations of organics. Similar to the previously observed formation of polycatechol and polyguaiacol in reactions of Fe(III) with catechol and guaiacol,[31] the formation of particles reported herein could account for new pathways that lead to SOA and brown carbon formation mediated by transition metals. This chemistry could also predict the reactivity of other atmospherically relevant and iron-containing surfaces that include soil, oceans, and built environments.

## ■ MATERIALS AND METHODS

**Chemicals.** All chemicals were used as received without further purification: fumaric acid (FA, *trans*-butenedioic acid, ≥ 99%, CAS: 110-17-8, Sigma-Aldrich), maleic acid (MaA, *cis*-butenedioic acid, 99%, CAS: 110-16-7, Sigma-Aldrich), succinic acid (SA, butanedioic acid, ≥ 99%, CAS: 110-15-6, Sigma-Aldrich), muconic acid (MA, *trans,trans*-2,4-hexadienedioic acid, 98%, CAS: 3588-17-8, Sigma-Aldrich), iron(II) fumarate (94%, CAS: 141-01-5, Alfa Aesar), and iron(III) chloride hexahydrate ($FeCl_3·6H_2O$, 97%, CAS: 10025-77-1, Sigma-Aldrich). Aqueous phase solutions were prepared by dissolving the chemicals in Milli-Q water (18.5 MΩcm) with the solutions' ionic strength adjusted to 0.01 M by adding potassium chloride (KCl powder, 99.5%, EM Science) in order to stabilize the pH reading. The pH was adjusted using stock solutions of hydrochloric acid (HCl 6 N, Ricca Chemical Company) and sodium hydroxide (NaOH pellets, 99−100%, EMD). The reactant concentrations were

chosen to be representative of concentrations expected for aerosol liquid water, with specific values depending on the type of the measurement.

**Spectrophotometry Experiments.** UV−vis spectra were collected using either a fiber optic UV−vis spectrometer (Ocean Optics USB 4000 UV−vis, 1 cm cuvette sample holder) or a Shimadzu UV-1800 spectrophotometer with a 1 cm quartz cuvette. In a typical experiment, 20 mL of the organic acid (0.1 mM, pH 5) was mixed with 0.25 mL $FeCl_3$ (pH ∼ 2) at a concentration that would yield the desired organic reactant:Fe molar ratio. The vial was wrapped in Al foil to avoid photochemical reactions. After a given reaction time, a 3 mL aliquot was taken using a syringe, without filtration, for collecting the UV−vis spectrum, unless otherwise specified.

**Dynamic Light Scattering (DLS) Experiments.** To monitor particle growth in solution, DLS experiments were performed on $FeCl_3$ reactions with 0.05 or 0.1 mM solutions of fumaric or muconic acids with starting organic reactant:Fe molar ratios 1:2 or 1:4. The reaction took place in a 1 cm Teflon capped-quartz cuvette with a Malvern Zetasizer Nano (ZEN3600) with a total measurement time up to 2 h.

**Dry Particle Characterization.** Particles that formed in solution as a result of the reaction between $FeCl_3$ and fumaric or muconic acids were collected on nylon membrane filters (0.2 $\mu$m pore size, 25 mm dia., EMD), and photographic images of the filters were taken using a digital camera. Mass yield experiments (as a measure of reaction efficiency) were performed after overnight reaction using 1:2 organic reactant:Fe molar ratio by weighing the filters before and after filtration followed by overnight drying. For these experiments, the concentration of the organics was 2.1 mM. The concentration was more than an order of magnitude larger than that used for UV−vis and DLS experiments in order to achieve a measurable mass of the precipitate. The particles were washed with Milli-Q water several times prior to drying in air. A suite of analytical techniques was used to characterize the dry particles including attenuated total internal reflectance (ATR-FTIR), thermogravimetric analysis (TGA), transmission electron microscopy (TEM) with diffraction, scanning transmission electron microscopy-energy dispersive X-ray spectroscopy (STEM-EDS) for elemental mapping, electron energy loss spectroscopy (EELS) for oxygen K-edge, and X-ray photoelectron spectroscopy (XPS) for iron oxidation state. Further details are provided in the Supporting Information (SI).

## ■ RESULTS AND DISCUSSION

**Optical Properties and Mechanism of Particle Formation.** Figure 1a and b show photographs of the mixtures of aqueous $FeCl_3$ with fumaric acid and muconic acid after 1 min, 1 h, and 24 h of reaction. The orange color development and colloid formation shown in Figure 1a and b were reproducibly observed upon the dark reaction of aqueous $FeCl_3$ with fumaric and muconic acid under acidic conditions and in the absence of intentionally added oxidants such as $H_2O_2$. To speed up complete dissolution of these acids, stock standard organic solutions were prepared at pH 5, above the second $pK_a$ for both diacids (relevant $pK_a$ values are listed in Figure 1). Upon addition of the acidic $FeCl_3$ solution to result in 1:2 and 1:4 organic reactant:Fe molar ratios, the solution pH dropped to around 3, and the color developed quickly as seen in the photographs already after 1 min of reaction. Particle formation was also observed with 2:1 and 4:1 organic reactant:Fe molar ratios with excess organics. However, reactions with excess iron were
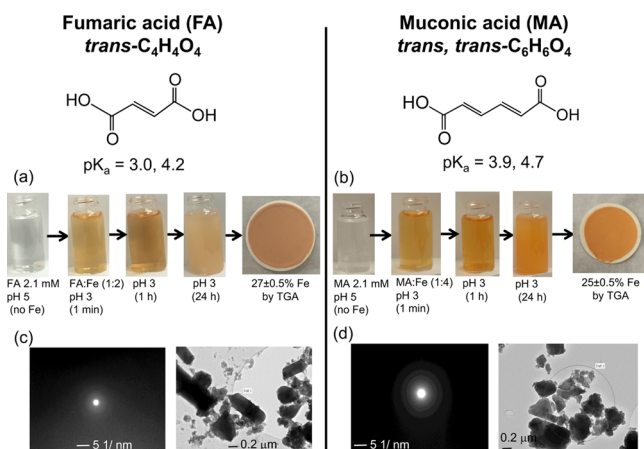
**Figure 1.** Dark reaction of fumaric acid (FA, panels, left) and muconic acid (MA, panels, right) with FeCl$_3$ at pH 3: (a,b) digital images of 1:2 organic reactant/Fe molar ratio of unfiltered solutions as a function of time and particles on filters after 24 h reaction time and (c,d) TEM images with diffraction of dry Fe-polyfumarate and Fe-polymuconate particles.

explored in more detail since these solutions are most sensitive to changes in levels of dissolved oxygen. The molar ratios for excess iron or excess organics cover the possibilities of such conditions in atmospheric particles at various stages of the aging process. Control experiments were conducted where the same volume of the organic acids was mixed with the background solution containing no Fe at the pH values listed above to confirm no precipitate formation under these conditions. Photographs of reaction solutions were taken for up to 24 h, where it could be clearly seen that they become progressively turbid. The concentrations were relatively high to mimic interfacial regions on surfaces where organic compounds are enriched. To the best of our knowledge, there have been no direct measurements of acids or iron concentration in water adsorbed on atmospheric particles. We inferred that the lower solvent to solute ratio at the interface would result in concentration of acids and iron in the lower millimolar range relative to their micromolar in bulk cloud and fog droplets.[41,42]

It is important to emphasize here that the aqueous solutions were exposed to air, and hence, dissolved O$_2$ can act as an oxidant. The level of dissolved O$_2$ in these experiments was quantified at $11 \pm 2$ mg L$^{-1}$ (or ppm). Bubbling N$_2$ gas into the reactant solutions prior to mixing for 1 h reduced the level of dissolved O$_2$ to $3 \pm 2$ ppm. Longer bubbling times up to 2 h did not significantly reduce this value further. Under these reduced dissolved O$_2$ conditions, mixing 2.1 mM organic reactants with FeCl$_3$ to end up in a 1:2 organic reactant:Fe molar ratio showed color change and colloidal particle formation similar to what is observed in Figure 1a and b. This control experiment showed that either relatively small quantities of dissolved O$_2$, below the detection limit of the dissolved O$_2$ electrode, were needed to drive the chemistry reported herein or that dissolved O$_2$ did not play a role in particle formation.

To better quantify changes to optical properties, Figure 2 shows time-dependent UV−vis spectra collected for unfiltered reaction solutions at 21-fold lower organic reactant concentrations than those used in Figure 1a and b. As reference, spectra for standard solutions of the reactants at their initial pH are also shown. These UV−vis spectra of the reaction mixture have contributions from particles and soluble reactants and products.
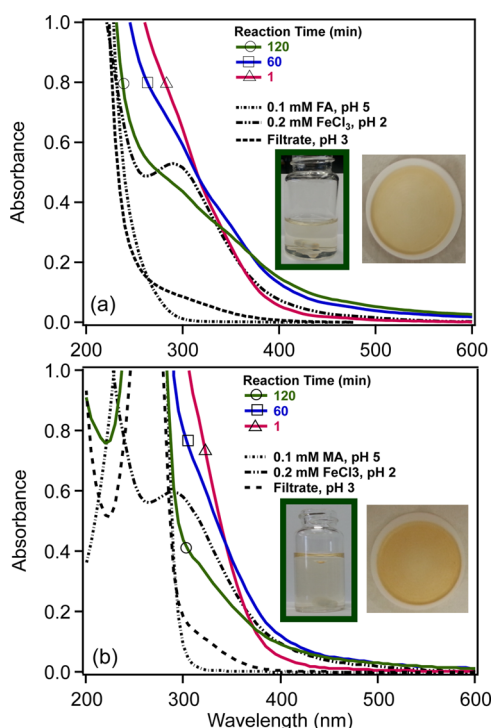


**Figure 2.** Time-dependent UV−vis spectra of unfiltered solutions following reaction of (a) FA and (b) MA with FeCl$_3$ at pH 3. For comparison, spectra of standard reactant solutions are also shown. The insets show digital images of the unfiltered solution after 120 min reaction time, which was filtered to record spectrum of the filtrate. The particles collected on the filter are shown as well. The empty markers are added as tags to spectra collected as a function of time.

The inset in Figure 2 shows photographs of the reaction solution after 2 h, which was filtered to obtain a spectrum of the filtrate, and the particles on the filter. The faint yellow color observed in these photographs compared to the much darker color in Figure 1a and b is a result of the 21-fold dilution of both reactant concentrations. These UV−vis experiments clearly showed that colloidal particles did form at organic reactant concentrations as low as 0.1 mM. The spectra of reaction solutions were red-shifted by nearly 100 nm relative to those collected for the initial organic reactants with absorbance bands that extend to 500 nm. Difference spectra obtained by subtracting the FeCl$_3$ reactant spectrum from those collected for the unfiltered reaction solution after 120 min are shown in Figure S1, which amplified the absorption bands at 370 nm. These bands appeared at a wavelength that is too high to be assigned to *d-d* transitions in Fe(III) aqueous species.[8] As supported by experimental evidence below, the bands at 370 nm were assigned to $\pi-\pi^*$ transitions in C=C groups of Fe-polyfumarate and Fe-polymuconate back-bone structures. In addition, the spectra of the filtrate solution in Figure 2a and b showed a residual feature between 300 and 400 nm, which likely originates from unreacted Fe(OH)$^{2+}$(aq) species since these experiments were conducted under excess Fe(III) conditions.

Figure 3 shows representative scattering intensity-weighted particle size distributions from the DLS experiments, plotted as a function of reaction time. The organic reactant concentrations used in these experiments (0.05 or 0.1 mM) were similar to those used for the UV−vis experiments because DLS operates best under dilute conditions. But even in these dilute solutions, polydisperse particles formed quickly and grew to particle sizes
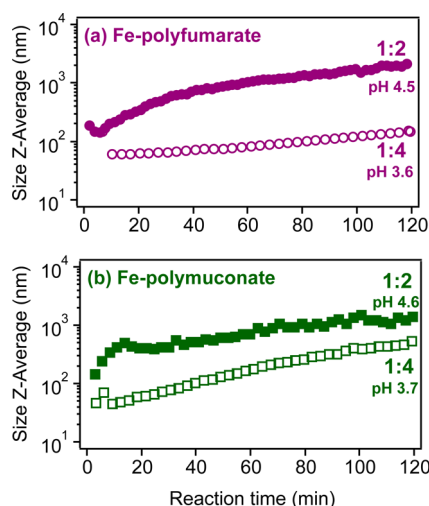
**Figure 3.** Scattering intensity-weighted particle size distributions from the DLS measurements of (a) Fe-polyfumarate and (b) Fe-polymuconate as a function of reaction time during the dark reaction of 0.05 mM FA and MA with $FeCl_3$ that resulted in either 1:2 or 1:4 organic reactant:Fe molar ratios. The pH in the figure is for the reaction solutions at 120 min.

greater than 100 nm in hydrodynamic size after half an hour of reaction. At longer reaction times above 120 min, there was clear evidence of sedimentation out of the solution (not shown) manifested by the decrease in the apparent particle size with time as the largest particles sedimented below the observation volume. The DLS measurements fully confirmed the UV−vis and visual observations that reactions of FA and MA with $FeCl_3$ efficiently produced water-insoluble particles. The growth rate of these particles appeared to depend on the final organic reactant:Fe molar ratio and pH. The effect of pH is complicated since it affects both the ionization state of the organic precursor and the speciation of iron in solution. The difference in pH of solutions containing 1:2 and 1:4 organic reactant:Fe molar ratios resulted from the different amounts of concentrated $FeCl_3$ solutions added to achieve the targeted ratio. Concentrated $FeCl_3$ solutions were very acidic (pH < 2), whereas the organic solutions were kept at pH 5. To achieve a 1:2 organic reactant:Fe molar ratio, a smaller volume of the $FeCl_3$ solution was added to organic standard solutions adjusted and kept at pH 5 than that added to achieve a 1:4 organic reactant:Fe molar ratio. The DLS results in Figure 3 show a higher growth rate for 1:2 relative to 1:4 molar ratio solutions suggesting a strong preference for more basic pH. Indeed, in a separate experiment where a pH 3.5 stock standard fumarate solution (1 mM) was mixed with $FeCl_3$ to result in 1:4 organic reactant:Fe molar ratio did not result in any observable particle formation after 120 min.

As stated in the Introduction, amorphous polymers or MOFs were reported from metal-catalyzed polymerization of FA and MA in the aqueous phase. The approximate formula reported in the patent by Apblett[34] was $Fe(O_2CCH=CHCO_2)\cdot1.5H_2O$ with a structure shown in Figure S2a. Figure S2b shows one side of the repeating unit in the MOF structure of MIL-88A reported by Lin et al.,[35] and Figure S2c shows the structure of polymers from the reaction of a mixture of *cic,cis*-muconic acid, succinic acid, and dialcohol oligomers using Ti(IV) butoxide as a transesterfication catalyst.[36] In these structures, the carboxylate ends of the FA or MA complex to the metal cations. Figure S2d shows the structure of the standard compound Fe(II) fumarate, which contains low spin state Fe(II) ions with two unpaired

electrons pointing toward a coordination polyhedron.[43,44] To check if the double bonds between the carboxylate groups were involved in the polymerization reactions under our reactions conditions of pH 3, room temperature, and with dissolved oxygen and $FeCl_3$, control experiments were conducted with MaA and SA. Figure S3 shows digital photos of solutions after reaction with $FeCl_3$. Color change was observed for both cases, however, filtration after 24 h of reaction with MaA at a 1:2 organic:Fe molar ratio showed very little to no particles on the filter. This suggests that the *cis* structure of the butenedioic acid was slower to either complex to Fe(III) or polymerize than the *trans* structure, presumably due to steric hindrances of adjacent carboxylate groups. As for SA, color change observed upon reaction with Fe(III) was mostly due to the formation of stable and soluble iron succinate complexes.[45,46] Hence, results from these experiments suggest that the C=C bonds present in FA, MA, and MaA played an important role in the mechanism of polymer formation in the presence of Fe(III) and dissolved oxygen. It is likely that the shape and energy spacing of the molecular orbitals in the organic molecules containing C=C bonds as opposed to C−C bonds favors complexation and ligand exchange with hydrated iron hydroxide species. Such differences in the electronic structure of organic precursors drive either polymeric formation with iron centers as linkers between organic molecules or soluble iron-organic molecules. The use of theoretical methods for calculating electronic density maps and energy of molecular orbitals for the systems studied herein would further our understanding of the mechanism. On the basis of the characterization of the dry particles, the chemical structure of the amorphous polymeric particles formed under our experimental conditions is discussed below and shown in Figure S4.

**Characterization of Dry Particles.** Samples collected for characterization were obtained by filtration of the reaction mixtures after 24 h as shown in Figure 1a and b. Concentration of the organic reactants was 2.1 mM, similar to that shown in Figure 1a and b, with $FeCl_3$ concentrations resulting in 1:2 and 1:4 organic reactant:Fe molar ratios using FA and MA, respectively. Particles on the filters were washed multiple times with Milli-Q water followed by overnight drying at room temperature. Weighing of the filters before and after the experiment permitted determination of the particle yield. Mass yield was calculated relative to the initial mass of the organic precursor (yield = [mass of particles/mass of organic precursor] × 100%) and found to be 84 ± 6% for Fe-polyfumarate and 52 ± 6% for Fe-polymuconate. These numbers suggest that water-soluble and colorless FA and MA could be converted to water-insoluble and colored products with high efficiency in the presence of excess Fe. We note that OH or ozone oxidation of MA and FA would instead produce water-soluble products that do not absorb visible light, so the Fe-mediated chemistry opens up unique pathways for processing of these diacids.

In other sets of experiments, the particles were scraped off the filters using a spatula for TEM, STEM-EDS, TGA, XPS, and EELS analyses. Figure 1c and d shows representative TEM images with diffraction of the dry Fe-polyfumarate and Fe-polymuconate particles. The former had a mixture of rod- and spherical-like particles, whereas the latter was dominated by irregular-shaped particles. The reproducible lack of diffraction patterns as shown in the images in Figure 1c and d confirmed that these particles were amorphous, which was also confirmed in independent micro-XRD particle analysis. Elemental mapping images using STEM-EDS are shown in Figure S5. For accuracy, the color intensity was normalized for relative comparisons of the

concentration of elements. Figure S5a shows that the Fe-polyfumarate nanorods are rich in Fe and O and have little to no C and Cl. These nanorods are attached to agglomerates, which are visible in the black and white image. The Fe-polymuconate particles in Figure S5b showed higher concentrations of Fe, O, and C and not too much Cl.

In addition, the iron content of Fe-polyfumarate and Fe-polymuconate was determined through TGA analysis. Figure S6 shows TGA curves for the polymers prepared herein and standard materials that include reactant organic acids FA and MA, $FeCl_3 \cdot 6H_2O$, and Fe(II) fumarate. The thermal decomposition of FA and MA standards showed complete degradation by 280 °C, whereas all samples containing iron had a residual weight at 800 °C. Detailed analysis of the thermal decomposition of standard compounds $FeCl_3 \cdot 6H_2O$[47] and Fe(II) fumarate[48] showed that hematite ($\alpha$-$Fe_2O_3$) forms at the highest temperatures. Table S1 lists thermal decomposition reactions for the materials studied herein. On the basis of the observed residual weight in Figure S6 of the standard compounds, the percentage of Fe and molar weight of the samples could be calculated, which matched those calculated from the chemical formula for the Fe-containing standard compounds. The percentage of Fe (26.7% and 24.8%, respectively) and effective molar weights (209.7 and 225.9 g $mol^{-1}$, respectively) were calculated for Fe-polyfumarate and Fe-polymuconate. Given the molar weights of fumarate ($C_4O_4H_2^{2-}$, 114 g $mol^{-1}$), muconate ($C_6O_4H_4^{2-}$, 140 g $mol^{-1}$), and Fe (56 g $mol^{-1}$), the chemical formulas for the smallest repeated units consistent with the percentage of Fe calculated above are $[C_4O_4H_2-Fe(H_2O)_2]$ in Fe-polyfumarate and $[C_6O_4H_4-Fe(H_2O)_2]$ in Fe-polymuconate, similar to the structure shown in Figure S2a. We assume that the Fe atoms maintain their normal coordination number of 6, and they can be either Fe(III) or Fe(II). In the case of Fe(III), the extra charge is compensated by replacing one of the $H_2O$ in formulas above by $OH^-$ (TGA analysis is not sensitive enough to distinguish between $H_2O$ and $OH^-$). Some of the OH could also be substituted for $Cl^-$, which explains the appearance of Cl in the elemental map of Figure S5.

The oxidation state of Fe in the Fe-polyfumarate and Fe-polymuconate samples was investigated using XPS, and results were compared to those obtained for Fe(II) fumarate as shown in Figure S7 and summarized in Table 1. Comparison of the Fe 2p

peaks with values reported for standard compounds containing Fe(III) and Fe(II) are also shown in Table 1. These compounds include iron (oxyhdyro)oxides and MOFs. Spectra collected for the Fe 2p peaks were slightly blue-shifted relative to those observed for Fe(II) fumarate. The dominance of Fe(II) in the Fe(II) fumarate standard compound gave rise to the feature at 713.9 eV. Grosvenor et al.[49] reported detailed analysis of the multiplet splitting of Fe 2p peaks in the XPS spectra for iron (oxyhdyro)oxides containing Fe(III) and Fe(II) as shown in Table 1. Similar results were reported by Yamashita and Hayes for iron oxidation states in oxide materials.[50] For compounds containing organics, Table 1 also lists a number of studies reported the chemical state of Fe in MOFs such as MIL-53(Fe) with terephthalate linkers,[51] MIL-100(Fe) with benzene-1,3,5-tricarboxylate (BTC) linkers,[52,53] and MIL-88(Fe) with fumarate linkers.[35] In these MOFs, the Fe centers are covalently bonded to the organic linkers, yet causing no ligand to metal charge transfer that would reduce Fe(III). The Fe 2p$_{3/2}$ peaks for the amorphous Fe-polyfumarate and Fe-polymuconate appear in between those assigned to Fe(III) and Fe(II) in the above standard crystalline compounds suggesting a different coordination environment for iron in the polymeric materials obtained herein.

Moreover, the bonding environment of oxygen atoms was probed using EELS O-K edge spectra, which were collected for the Fe-polyfumarate and Fe-polymuconate particles and compared to standard compounds Fe(II) fumarate, FA, and MA (Figure S8). The presence of iron affected the structure of the O−K edge peaks in the 500−570 eV region. According to a survey of iron−oxygen compounds that include FeO, $Fe_3O_4$, $\alpha$-$Fe_2O_3$, and $\gamma$-$Fe_2O_3$ by Colliex et al.,[54] the oxygen K edge displays four distinct features: (a) a prepeak below 530 eV that increases in intensity from FeO to $Fe_2O_3$, (b) a dominant feature around 540 eV, (c) a weak maximum in the 545−550 eV region that differs in structure among different iron oxide phases, and (d) a major broad feature between 560 and 565 eV. Spectra shown in Figure S8a display features a, b, and d. These peaks appeared more intense in the standard Fe(II) fumarate spectrum than in Fe-polyfumarate and Fe-polymuconate spectra. When compared to spectra collected for reactants FA and MA in Figure S8b, it was observed that peaks a and b were more pronounced and appeared in the same location for Fe-polyfumarate and FA. This suggests little influence of iron on the bonding environment for oxygen in the polymeric particles. In the case of Fe-polymuconate and MA, peak b appeared red-shifted to 537 eV, and peak c became pronounced in the spectrum of the former. This observation suggested more extensive changes to the oxygen bonding network in the Fe-polymuconate particles compared to MA and Fe-polyfumarate given its size and conjugated network. In light of the above analysis, the influence of iron on the electronic structure of products varies with the structure of the organic compound used.

Moreover, Figure 4a shows ATR-FTIR spectra of solid Fe-polyfumarate and Fe-polymuconate formed in reactions of Fe(III) with fumarate and muconate, respectively. These spectra were compared with those recorded for reference materials: solid and dry film of Fe(II) fumarate and aqueous phase fumarate and muconate as a function of pH (Figure 4b). The 2000−1000 $cm^{-1}$ spectral range contains stretching vibrations of carbonyl, $\nu$(C═O) (1800−1700 $cm^{-1}$), $\nu$(C═C) (1680−1600 $cm^{-1}$), asymmetric and symmetric stretching modes of − C(O)O− and − $CO_2^-$ functional groups, $\nu$($CO_2$) (1600−1270 $cm^{-1}$), and $\nu$(C−O) (1220−1150 $cm^{-1}$). Examining the spectra of reference compounds in Figure 4b showed that peaks for solid Fe(II)

**Table 1. Location of Fe 2p Peaks in XPS spectra of Fe-Polyfumarate, Fe-Polymuconate, and Reference Compounds**

| Chemical Compound | Location (eV) | Assignment | Ref |
|---|---|---|---|
| Fe-polyfumarate | 710.6, 724.2 | Fe 2p$_{3/2}$ | This study |
| Fe-polymuconate | 710.5, 724.2 | Fe 2p$_{3/2}$ | This study |
| Fe(II) fumarate | 710.0, 713.9 | Fe(II) 2p$_{3/2}$ | This study |
| Fe(II) fumarate | 723.0 | Fe(III) 2p$_{1/2}$ | This study |
| $\alpha$-$Fe_2O_3$ | 710.8 ± 0.2 | Fe(III) 2p$_{3/2}$ | 49, 50 |
| $\gamma$-$Fe_2O_3$ | 711.0 ± 0.2 | Fe(III) 2p$_{3/2}$ | 49, 50 |
| $\alpha$-FeOOH | 711.4 ± 0.2 | Fe(III) 2p$_{3/2}$ | 49, 50 |
| $Fe_3O_4$ | 709.0 | Fe(II) 2p$_{3/2}$ | 49, 50 |
| $Fe_3O_4$ | >720 | Fe(III) 2p$_{1/2}$ | 49, 50 |
| $Fe_{1.1}O$ | 709.5 | Fe(II) 2p$_{3/2}$ | 49, 50 |
| $Fe_{1.1}O$ | >720 | Fe(III) 2p$_{1/2}$ | 49, 50 |
| MIL-53(Fe) | 711.9, 725.7 | Fe 2p$_{3/2}$ | 51 |
| MIL-100(Fe) | 710.8, 724.8 | Fe 2p$_{3/2}$ | 39 |
| MIL-88(Fe) | 711.4, 725.2 | Fe 2p$_{3/2}$ | 35 |
| Fe-BTC | 711.8, 725.6 | Fe 2p$_{3/2}$ | 40 |
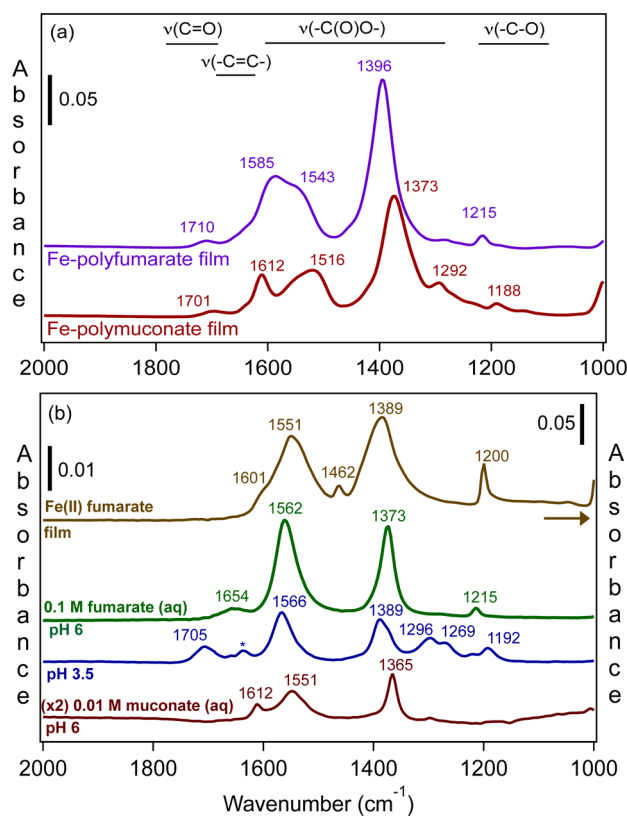
**Figure 4.** ATR-FTIR absorbance spectra of (a) amorphous Fe-polyfumarate and Fe-polymuconate films deposited on a ZnSe ATR crystal from a water/ethanol slurry followed by drying overnight and (b) standard compounds: solid Fe(II) fumarate, fumarate aqueous solutions at pH 6 and 3.5 of fully deprotonated, and monodeprotonated species, and muconate aqueous solutions at pH 6 of fully deprotonated species. "∗" is water bending mode from incomplete subtraction.

fumarate are broader than those for the organic monomers in the aqueous phase due to the rigid structure of the former. A similar spectrum was published for solid Fe(II) fumarate using KBr pellets in transmission FTIR.[43] The crystalline structure and magnetic susceptibility measurements of solid Fe(II) fumarate showed that it formed a macromolecular chain with Fe(II) ions appearing in low spin state.[43] The carbonyl mode was absent from its spectrum confirming that carboxylate groups chelate Fe(II) in a bidentate configuration. Similar features were observed in the IR spectrum of Fe(III) fumarate polymer reported by Apblett.[34] For comparison with monomers, the spectra of aqueous phase fumarate in Figure 4b showed characteristic features of fully deprotonated species at pH 6 and the absence of the carbonyl feature due to resonance within carboxylate groups. The spectrum collected at pH 3.5 has contributions from singly protonated fumarate, hence explaining the carbonyl feature at 1705 cm$^{-1}$, $v(CO_2^-)$ at 1296 and 1269 cm$^{-1}$, and $v(COH)$ at 1192 cm$^{-1}$. Similarly, the spectrum of aqueous phase muconate at pH 6 showed features characteristic of fully deprotonated species. In addition to the $v_{as}(CO_2^-)$ and $v_s(CO_2^-)$ at 1551 and 1365 cm$^{-1}$, the $v(C=C)$ mode appears at 1612 cm$^{-1}$, which was not observed in the aqueous fumarate spectra. Attempts to collect a spectrum at pH 4 were not successful because of precipitation even at low concentrations.

Hence, based on the above spectral analysis of reference materials, Figure S4 shows the proposed structure of (a) Fe-polyfumarate and (b) Fe-polymuconate. The features observed

in the spectrum of Fe-polyfumarate in Figure 4a suggested that some of the carboxylate groups were not coordinated to Fe in a bidentate fashion like Fe(II) fumarate because of (a) the presence of $v(C=O)$ at 1710 cm$^{-1}$, albeit at low intensity, (b) uncomplexed $v(C-O)$ at 1215 cm$^{-1}$, which is at the same location for uncomplexed aqueous fumarate at pH 6, and (c) significant asymmetry in intensity of peaks assigned to $v(CO_2^-)$ between 1600 and 1300 cm$^{-1}$ that does not resemble those observed for fully deprotonated fumarate and Fe(II) fumarate film. Hence, some of the fumarate molecules are likely to be coordinated to Fe(III) in a monodentate fashion, which will result in a carbonyl feature, but the majority form an amorphous network with pores where residual Fe(III) and Cl$^-$ ions are trapped. This interpretation would explain the Fe and Cl signal in the STEM-EDS images of Fe-polyfumarate and also supports the trends observed in the XPS (Figure S7) and EELS (Figure S8) spectra when compared to reference compounds. As for Fe-polymuconate, the spectrum in Figure 4a also suggested binding to Fe(III) in a monodentate fashion given the visibility of $v(C=O)$ at 1701 cm$^{-1}$, which ruled out bidentate chelation. The appearance of $v(C-O)$ at 1188 cm$^{-1}$, which did not exist in the spectrum of the monomer at pH 6 (Figure 4b), was likely due to CO−Fe bond. This interpretation explained the appearance of the peak at 545.2 eV in the EELS spectrum (Figure S8).

The results presented herein are significant and will help fill the gap in our understanding of the bulk and surface chemistry of iron in atmospherically relevant systems. As detailed in the Introduction, field-collected aerosols containing iron from natural and anthropogenic sources are ubiquitous, and these are the same sources that emit VOCs leading to SOA formation. Hence, the plausibility for VOC oxidation products to condense on iron-containing aerosols is high, which makes the pathway for particle formation presented herein likely under atmospheric conditions. We showed that the dark reaction of *trans*-C4 and C6 unsaturated diacids with Fe(III) under acidic conditions and in the absence of any added oxidants resulted in the formation of insoluble and amorphous polymeric particles containing iron centers with intermediate oxidation states between Fe(III) and Fe(II) of standard metal oxides and metal−organic frameworks. The particles were mostly rod-shaped for Fe-polyfumarate and irregular-shaped for Fe-polymuconate. The growth rate of the particles was faster at pH > 4 and 1:2 organic to iron molar. Control experiments using the *cis*-isomer, maleic acid, and a saturated C4 diacid, succinic acid, did not produce particles on the same time scale as fumaric and muconic acids highlighting structural roles in the mechanism of particle formation. The effect of abundant inorganic species such as sulfate or nitrate or organics species such as oxalate on the results presented herein is currently underway in our laboratories, in addition to experiments at pH values typical of fine aerosols (pH < 2).[55]

The visible light absorption by the resulting insoluble material has implications for the climate, which could be quantified with the help of bulk mass-normalized absorption coefficient (MAC) of the organics as follows:[4]

$$MAC(\lambda) = \frac{A(\lambda) \times \ln(10)}{l \times C_{mass}} \tag{1}$$

where $A(\lambda)$ is base-10 absorbance, $l$ is the cuvette path length, and $C_{mass}$ is the initial mass concentration of dissolved fumaric or muconic acids. Figure S9 shows MAC plots for the dark reaction of 0.1 mM fumaric and muconic acids with 0.2 mM FeCl$_3$ at pH 3 as a function of time for unfiltered solutions, i.e., with particles

contributing to the absorption. At 365 and 405 nm, where absorption coefficients of ambient particles are frequently measured, the observed MAC values after 1 h of reaction were as high as $\sim 6$ and $\sim 2$ m$^2$ g$^{-1}$, respectively. This is of the same order of magnitude as MAC values reported for biomass burning aerosols ($\sim 1$ m$^2$ g$^{-1}$ in the near-UV range)[56] and for black carbon[57] (7.5 m$^2$ g$^{-1}$ for uncoated soot). In the visible range, the observed MAC values drop to $\sim 1$ m$^2$ g$^{-1}$ at 500 nm, but they still remain comparable to or higher than the typical MAC values for biomass burning aerosols. Therefore, the metal driven transformation of SOA products is potentially an important pathway for the formation of secondary "brown carbon".

Moreover, the chemistry presented herein provides molecular level details to processes that could take place in acidic multicomponent systems containing organics and iron. Reactions like the one presented herein will make aqueous phase Fe(III) less available to drive bulk chemistry since it is part of the insoluble particles. Iron centers in the amorphous structures of Fe-polyfumarate and Fe-polymuconate could act as catalysts for the dark and photochemical production of reactive oxygen species (ROS)[8] such as OH and $H_2O_2$, adsorption of oxyanions such as sulfate, and reduction of NO$_x$ in the presence of ammonia. These chemical processes will depend on the amount of "adsorbed water" and aerosol liquid water. This has been demonstrated in a number of studies that employ iron-containing MOFs.[34,35,51,52,58,59] Similar to polycatechol and polyguiacol,[31] the high hydrophobicity of Fe-polyfumarate and Fe-polymuconate will likely drive their enrichment at surfaces of aerosols with direct consequences on their (likely poor) ability to act as cloud and ice condensation nuclei.[60,61]

## ■ ASSOCIATED CONTENT

### Ⓢ Supporting Information

The Supporting Information is available free of charge on the ACS Publications website at DOI: 10.1021/acs.est.7b01826.

> Detailed experimental procedures and figures and tables showing data analysis. (PDF)

## ■ AUTHOR INFORMATION

### Corresponding Author

*Phone: (519)884-0710, ext. 2873. Fax: (519)746-0677. E-mail: halabadleh@wlu.ca.

### ORCID Ⓘ

Sergey A. Nizkorodov: 0000-0003-0891-0052
Hind A. Al-Abadleh: 0000-0002-9425-0646

### Notes

The authors declare no competing financial interest.

## ■ REFERENCES

(1) Moise, T.; Flores, J. M.; Rudich, Y. Optical properties of secondary organic aerosols and their changes by chemical processes. *Chem. Rev.* **2015**, *115* (10), 4400−4439.

(2) Flores, J. M.; Zhao, D. F.; Segev, L.; Schlag, P.; Kiendler-Scharr, A.; Fuchs, H.; Watne, Å. K.; Bluvshtein, N.; Mentel, T. F.; Hallquist, M.; Rudich, Y. Evolution of the complex refractive index in the UV spectral region in ageing secondary organic aerosol. *Atmos. Chem. Phys.* **2014**, *14* (11), 5793−5806.

(3) Lambe, A. T.; Cappa, C. D.; Massoli, P.; Onasch, T. B.; Forestieri, S. D.; Martin, A. T.; Cummings, M. J.; Croasdale, D. R.; Brune, W. H.; Worsnop, D. R.; Davidovits, P. Relationship between oxidation level and optical properties of secondary organic aerosol. *Environ. Sci. Technol.* **2013**, *47* (12), 6349−6357.

(4) Laskin, A.; Laskin, J.; Nizkorodov, S. A. Chemistry of atmospheric brown carbon. *Chem. Rev.* **2015**, *115* (10), 4335−4382.

(5) Andreae, M. O.; Gelencsér, A. Black carbon or brown carbon? The nature of light-absorbing carbonaceous aerosols. *Atmos. Chem. Phys.* **2006**, *6* (10), 3131−3148.

(6) Ziemann, P. J.; Atkinson, R. Kinetics, products, and mechanisms of secondary organic aerosol formation. *Chem. Soc. Rev.* **2012**, *41*, 6582−6605.

(7) Zhang, R.; Khalizov, A.; Wang, L.; Hu, M.; Xu, W. Nucleation and growth of nanoparticles in the atmosphere. *Chem. Rev.* **2012**, *112* (3), 1957−2011.

(8) Al-Abadleh, H. A. A review on the bulk and surface chemistry of iron in atmospherically-relevant systems containing humic like substances. *RSC Adv.* **2015**, *5*, 45785−45811.

(9) Maher, B. A.; Prospero, J. M.; Mackie, D.; Gaiero, D.; Hesse, P. P.; Balkanski, Y. Global connections between aeolian dust, climate and ocean biogeochemistry at the present day and at the last glacial maximum. *Earth-Sci. Rev.* **2010**, *99*, 61−97.

(10) Mahowald, N.; Baker, A. R.; Bergametti, G.; Brooks, N.; Duce, R. A.; Jickells, T. D.; Kubilay, N.; Prospero, J. M.; Tegen, I. Atmospheric global dust cycle and iron inputs to the ocean. *Global Biogeochem. Cycles* **2005**, *19*, 1−15.

(11) Conway, T. M.; John, S. G. Quantification of dissolved iron sources to the North Atlantic Ocean. *Nature* **2014**, *511*, 212−215.

(12) Sedwick, P. N.; Sholkovitz, E. R.; Church, T. M. Impact of anthropogenic combustion emissions on the fractional solubility of aerosol iron: Evidence from the Sargasso Sea. *Geochem., Geophys., Geosyst.* **2007**, *8*, Q10Q06.

(13) Guieu, C.; Bonnet, S.; Wagener, T.; Loye-Pilot, M.-D. Biomass burning as a source of dissolved iron to the open ocean? *Geophys. Res. Lett.* **2005**, *32*, L19608.

(14) Ito, A. Atmospheric Processing of Combustion Aerosols as a Source of Bioavailable Iron. *Environ. Sci. Technol. Lett.* **2015**, *2* (3), 70−75.

(15) Oakes, M.; Weber, R. J.; Lai, B.; Russell, A.; Ingall, E. D. Characterization of iron speciation in urban and rural single particles using XANES spectroscopy and micro X-ray fluorescence measurements: investigating the relationship between speciation and fractional iron solubility. *Atmos. Chem. Phys.* **2012**, *12*, 745−756.

(16) Butler, A. J.; Andrew, M. S.; Russell, A. G. Daily sampling of PM2.5 in Atlanta: Results of the first year of the assessment of spatial aerosol composition in Atlanta study. *J. Geophys. Res.* **2003**, *108* (D7), 8415.

(17) Hoffmann, P.; Dedik, A. N.; Ensling, J.; Weinbruch, S.; Weber, S.; Sinner, T.; Gutlich, P.; Ortner, H. M. Speciation of iron in atmospheric aerosol samples. *J. Aerosol Sci.* **1996**, *27*, 325−327.

(18) Johansen, A. M.; Siefert, R.; Hoffmann, M. R. Chemical composition of aerosols collected over the tropical North Atlantic ocean. *J. Geophys. Res-Atmos.* **2000**, *105*, 15277−15312.

(19) Liu, W.; Wang, Y. H.; Russell, A.; Edgerton, E. S. Atmospheric aerosol over two urban-rural pairs in the southeastern United States: Chemical composition and possible sources. *Atmos. Environ.* **2005**, *39*, 4453−4470.

(20) Oakes, M.; Rastogi, N.; Majestic, B. J.; Shafer, M.; Schauer, J. J.; Edgerton, E. S.; Weber, R. J. Characterization of soluble iron in urban aerosols using near-real time data. *J. Geophys. Res.* **2010**, *115*, D15302.

(21) Ault, A. P.; Peters, T. M.; Sawvel, E. J.; Casuccio, G. S.; Willis, R. D.; Norris, G. A.; Grassian, V. H. Single-particle SEM-EDX Analysis of iron-containing coarse particulate matter in an urban environment: Sources and distribution of iron within Cleveland, Ohio. *Environ. Sci. Technol.* **2012**, *46*, 4331−4339.

(22) Guasco, T. L.; Cuadra-Rodriguez, L. A.; Pedler, B. E.; Ault, A. P.; Collins, D. B.; Zhao, D.; Kim, M. J.; Ruppel, M. J.; Wilson, S. C.; Pomeroy, R. S.; Grassian, V. H.; Azam, F.; Bertram, T. H.; Prather, K. A. Transition metal associations with primary biological particles in sea spray aerosol generated in a wave channel. *Environ. Sci. Technol.* **2014**, *48*, 1324−1333.

(23) Ault, A. P.; Moore, M. J.; Furutani, H.; Prather, K. A. Impact of emissions from the Los Angeles port region on San Diego air quality during regional transport events. *Environ. Sci. Technol.* **2009**, *43*, 3500−3506.

(24) Ault, A. P.; Gaston, C. J.; Wang, Y.; Dominguez, G.; Thiemens, M. H.; Prather, K. A. Characterization of the single particle mixing state of individual ship plume events measured at the port of Los Angeles. *Environ. Sci. Technol.* **2010**, *44*, 1954−1961.

(25) Deboudt, K.; Flament, P.; Choel, M.; Gloter, A.; Sobanska, S.; Colliex, C. Mixing state of aerosols and direct observation of carbonaceous and marine coatings on African dust by individual particle analysis. *J. Geophys. Res-Atmos.* **2010**, *115*, D24207.

(26) Takahama, S.; Gilardoni, S.; Russell, L. M. Single-particle oxidation state and morphology of atmospheric iron aerosols. *J. Geophys. Res.* **2008**, *113*, D22202.

(27) Schroth, A. W.; Crusius, J.; Sholkovitz, E. R.; Bostick, B. C. Iron solubility driven by speciation in dust sources to the ocean. *Nat. Geosci.* **2009**, *2*, 337−340.

(28) Shi, Z.; Krom, M. D.; Bonneville, S.; Benning, L. G. Atmospheric processing outside clouds increases soluble iron in mineral dust. *Environ. Sci. Technol.* **2015**, *49* (3), 1472−1477.

(29) Winton, V. H. L.; Edwards, R.; Bowie, A. R.; Keywood, M. D.; Williams, A. G.; Chambers, S. D.; Selleck, P. W.; Desservettaz, M.; Mallet, M. D.; Paton-Walsh, C. Dry season aerosol iron solubility in tropical northern Australia. *Atmos. Chem. Phys.* **2016**, *16*, 12829−12848.

(30) Nguyen, T. K. V.; Zhang, Q.; Jimenez, J. L.; Pike, M.; Carlton, A. G. Liquid Water: Ubiquitous contributor to aerosol Mass. *Environ. Sci. Technol. Lett.* **2016**, *3* (7), 257−263.

(31) Slikboer, S.; Grandy, L.; Blair, S. L.; Nizkorodov, S. A.; Smith, R. W.; Al-Abadleh, H. A. Formation of light absorbing soluble secondary organics and insoluble polymeric particles from the dark reaction of catechol and guaiacol with Fe(III). *Environ. Sci. Technol.* **2015**, *49*, 7793−7801.

(32) Jenkin, M. E.; Saunders, S. M.; Wagner, V.; Pilling, M. J. Protocol for the development of the Master Chemical Mechanism, MCM v3 (Part B): tropospheric degradation of aromatic volatile organic compounds. *Atmos. Chem. Phys.* **2003**, *3*, 181−193.

(33) Finlayson-Pitts, B. J.; Pitts, J. N., Jr. *Chemistry of the Upper and Lower Atmosphere*; Academic Press: New York, 2000.

(34) Apblett, A. W. Iron coordination polymers for adsorption of arsenate and phosphate. U.S. Patent US 2013/0292338 A1, 2013.

(35) Lin, K.-Y. A.; Chang, H.-A.; Hsu, C.-J. Iron-based metal organic framework, MIL-88A, as a heterogeneous persulfate catalyst for decolorization of Rhodamine B in water. *RSC Adv.* **2015**, *5*, 32520−32530.

(36) Rorrer, N. A.; Dorgan, J. R.; Vardon, D. R.; Martinez, C. R.; Yang, Y.; Beckham, G. T. Renewable unsaturated polyesters from muconic acid. *ACS Sustainable Chem. Eng.* **2016**, *4*, 6867−6876.

(37) Borras, E.; Tortajada-Genaro, L. A. Secondary organic aerosol formation from photo-oxidation of benzene. *Atmos. Environ.* **2012**, *47*, 154−163.

(38) Huang, M.; Lin, Y.; Huang, X.; et al. Chemical analysis of aged benzene secondary organic aerosol using aerosol laser time-of-flight mass spectrometer. *J. Atmos. Chem.* **2014**, *71*, 213−224.

(39) Cong, Z. Y.; Kawamura, K.; Kang, S. C.; Fu, P. Q. Penetration of biomass-burning emissions from South Asia through the Himalayas: New insights from atmospheric organic acids. *Sci. Rep.* **2015**, *5*, 9580.

(40) Kawamura, K.; Tachibana, E.; Okuzawa, K.; Aggarwal, S. G.; Kanaya, Y.; Wang, Z. F. High abundances of water-soluble dicarboxylic acids, ketocarboxylic acids and alpha-dicarbonyls in the mountaintop aerosols over the North China Plain during wheat burning season. *Atmos. Chem. Phys.* **2013**, *13*, 8285−8302.

(41) Ervens, B. Modeling the Processing of Aerosol and Trace Gases in Clouds and Fogs. *Chem. Rev.* **2015**, *115* (10), 4157−4198.

(42) Faust, B. C.; Hoigne, J. Photolysis of Fe (III)-hydroxy complexes as sources of OH radicals in clouds, fog and rain. *Atmos. Environ., Part A* **1990**, *24*, 79−89.

(43) Kapor, A. J.; Nikolic, L. B.; Nikolic, V. D.; Stankovic, M. Z.; Cakic, M. D.; Ilic, D. P.; Mladenovic-Ranisavljevic, I. I.; Ristic, I. S. The synthesis and characterization of iron(II) fumarate and its inclusion complexes with cyclodextrins. *Adv. Technol.* **2012**, *1*, 7−15.

(44) Skuban, S.; Dzomie, T.; Kapor, A.; Cvejic, Z.; Rakic, S. Dielectric and structural properties of iron- and sodium-fumarates. *J. Res. Phys.* **2012**, *36*, 21−29.

(45) Cmuk, P.; Piantanida, I.; Mlakar, M. Iron(III)-Complexes Engaged in the Biochemical Processes in Seawater. I. Voltammetry of Fe(III)-Succinate Complexes in Model Aqueous Solution. *Electroanalysis* **2009**, *21*, 2527−2534.

(46) Vukosav, P.; Mlakar, M. Iron(III)-organic complexes dissolved in seawater: Characterization of iron(III)-succinate and iron(III)-malate complexes in aqueous solution. *Rapp. Comm. int. Mer Médit.* **2010**, *39*, 321−321.

(47) Kanungo, S. B.; Mishra, S. K. Thermal dehydration and decomposition of FeCl$_3$.xH$_2$O. *J. Therm. Anal.* **1996**, *46*, 1487−1500.

(48) Nikumbh, A. K.; Phadke, M. M.; Date, S. K.; Bakare, P. P. Miissbauer spectroscopic and D.C. electrical conductivity study of the thermal decomposition of some iron(II) dicarboxylates. *Thermochim. Acta* **1994**, *239*, 253−268.

(49) Grosvenor, A. P.; Kobe, B. A.; Biesinger, M. C.; McIntyre, N. S. Investigation of multiplet splitting of Fe 2p XPS spectra and bonding in iron compounds. *Surf. Interface Anal.* **2004**, *36*, 1564−1574.

(50) Yamashita, T.; Hayes, P. Analysis of XPS spectra of Fe$^{2+}$ and Fe$^{3+}$ ions in oxide materials. *Appl. Surf. Sci.* **2008**, *254*, 2441−2449.

(51) Vu, T. A.; Le, G. H.; Dao, C. D.; Dang, L. Q.; Nguyen, K. T.; Nguyen, Q. K.; Dang, P. T.; Tran, H. T. K.; Duong, Q. T.; Nguyen, T. V.; Lee, G. D. Arsenic removal from aqueous solutions by adsorption using novel MIL-53(Fe) as a highly efficient adsorbent. *RSC Adv.* **2015**, *5*, 5261−5268.

(52) Zhu, B.-J.; Yu, X.-Y.; Jia, Y.; Peng, F.-M.; Sun, B.; Zhang, M.-Y.; Luo, T.; Liu, J.-H.; Huang, X.-J. Iron and 1,3,5-benzenetricarboxylic metal−organic coordination polymers prepared by solvothermal method and their application in efficient As(V) removal from aqueous solutions. *J. Phys. Chem. C* **2012**, *116*, 8601−8607.

(53) Lv, H.; Zhao, H.; Cao, T.; Qian, L.; Wang, Y.; Zhao, G. Efficient degradation of high concentration azo-dye wastewater by heterogeneous Fenton process with iron-based metal-organic framework. *J. Mol. Catal. A: Chem.* **2015**, *400*, 81−89.

(54) Colliex, C.; Manoubi, T.; Ortiz, C. Electron-energy-loss-spectroscopy near-edge fine structures in the iron-oxygen system. *Phys. Rev. B: Condens. Matter Mater. Phys.* **1991**, *44*, 11402−11411.

(55) Guo, H.; Xu, L.; Bougiatioti, A.; Cerully, K. M.; Capps, S. L.; Hite, J. R.; Carlton, A. G.; Lee, S.-H.; Bergin, M. H.; Ng, N. L.; Nenes, A.; Weber, R. J. Fine-particle water and pH in the southeastern United States. *Atmos. Chem. Phys.* **2015**, *15*, 5211−5228.

(56) Chen, Y.; Bond, T. C. Light absorption by organic carbon from wood combustion. *Atmos. Chem. Phys.* **2010**, *10* (4), 1773−1787.

(57) Bond, T.; Bergstrom, R. Light absorption by carbonaceous particles: an investigative review. *Aerosol Sci. Technol.* **2006**, *40* (1), 27−67.

(58) Dhakshinamoorthy, A.; Alvaro, M.; Horcajada, P.; Gibson, E.; Vishnuvarthan, M.; Vimont, A.; Greneche, J.-M.; Serre, C.; Daturi, M.; Garcia, H. Comparison of porous iron trimesates basolite F300 and MIL-100(Fe) as heterogeneous catalysts for Lewis acid and oxidation

reactions: roles of structural defects and stability. *ACS Catal.* **2012**, *2*, 2060−2065.

(59) Wang, P.; Zhao, H.; Sun, H.; Yu, H.; Chen, S.; Quan, X. Porous metal−organic framework MIL-100(Fe) as an efficient catalyst for the selective catalytic reduction of $NO_x$ with $NH_3$. *RSC Adv.* **2014**, *4*, 48912−48919.

(60) Taraniuk, I.; Graber, E. R.; Kostinski, A.; Rudich, Y. Surfactant properties of atmospheric and model humic-like substances (HULIS). *Geophys. Res. Lett.* **2007**, *34*, L16807.

(61) Dinar, E.; Taraniuk, I.; Graber, E. R.; Anttila, T.; Mentel, T. F.; Rudich, Y. Hygroscopic growth of atmospheric and model humic-like substances. *J. Geophys. Res.* **2007**, *112*, D05211.